ACS APPLIED MATERIALS & INTERFACES

www.acsami.org

Research Article

Deep Learning Accelerated Design of Mechanically Efficient Architected Materials

Sangryun Lee, Zhizhou Zhang, and Grace X. Gu*

Cite This: *ACS Appl. Mater. Interfaces* 2023, 15, 22543−22552

Read Online

ACCESS | Metrics & More | Article Recommendations | Supporting Information

ABSTRACT: Lattice structures are known to have high performance-to-weight ratios because of their highly efficient material distribution in a given volume. However, their inherently large void fraction leads to low mechanical properties compared to the base material, high anisotropy, and brittleness. Most works to date have focused on modifying the spatial arrangement of beam elements to overcome these limitations, but only simple beam geometries are adopted due to the infinitely large design space associated with probing and varying beam shapes. Herein, we present an approach to enhance the elastic modulus, strength, and toughness of lattice structures with minimal tradeoffs by optimizing the shape of beam elements for a suite of lattice structures. A generative deep learning-based approach is employed, which leverages the fast inference of neural networks to accelerate the optimization process. Our optimized lattice structures possess superior stiffness (+59%), strength (+49%), toughness (+106%), and isotropy (+645%) compared to benchmark lattices consisting of cylindrical beams. We fabricate our lattice designs using additive manufacturing to validate the optimization approach; experimental and simulation results show good agreement. Remarkable improvement in mechanical properties is shown to be the effect of distributed stress fields and deformation modes subject to beam shape and lattice type.

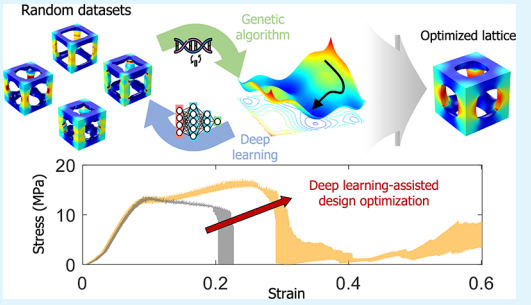

KEYWORDS: *lattice structures, deep learning, mechanical properties, additive manufacturing, genetic optimization*

INTRODUCTION

Lattice structures have a three-dimensional architecture in which struts or beams connect at joints and possess cubic symmetry in mechanical properties.[1−3] Since their architecture has highly efficient material distribution in a given three-dimensional space, lattice structures tend to have outstanding specific properties such as a high strength-to-weight ratio, stiffness-to-weight ratio, and energy absorption efficiency compared to other conventional engineering materials.[4−6] As a result, lattice structures have been widely adopted for many applications such as biomedical implants, aircraft, automobile chassis, and use in other metamaterials to utilize their novel lightweight properties.[7−9] For example, in automotive engineering, the lattice structure has been used for many automotive components including crash boxes,[10] engine hoods,[11] and arm design.[12] In the field of aerospace engineering, many applications have adopted the lattice structure, such as airfoils,[13] three-dimensional lattice-based energy absorption structures,[14] and vibration absorbing lattices.[15] Additionally, in biomedical applications, orthopedic implants have been designed by employing lattice structures in order to prevent the failure of the bone−implant interface.[3] However, also because of the inherent sparse structural properties of the lattice architecture, the lattice faces several challenges that should be considered.

First, the mechanical properties of the lattice structure, such as modulus or strength, are lower than those of the base material because of the inherent high void fraction of the lattice.[16,17] The origin of the limit stems from the tradeoff between void fraction and mechanical properties.[18,19] Second, since lattice structures can never achieve perfect isotropy, the mechanical properties of the lattice are orientation-dependent; they heavily depend on the direction of the applied load.[20−22] This high anisotropy of the lattice structure is a hurdle for several structural applications having uncertainty in loading and should ideally be mitigated. The last limitation for lattice structures is the oftentimes low toughness and small strain limit, resulting from the high stress concentration around the beam intersections at the joints, which causes catastrophic failure with large energy release when a crack nucleates.[23]

To overcome these limitations, many efforts over the past few decades have been devoted to tuning the spatial arrangement or shape of the beam elements in lattice structures. For instance, in the case of a body-centered (BC)

Received: February 25, 2023
Accepted: April 11, 2023
Published: April 27, 2023

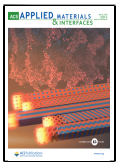

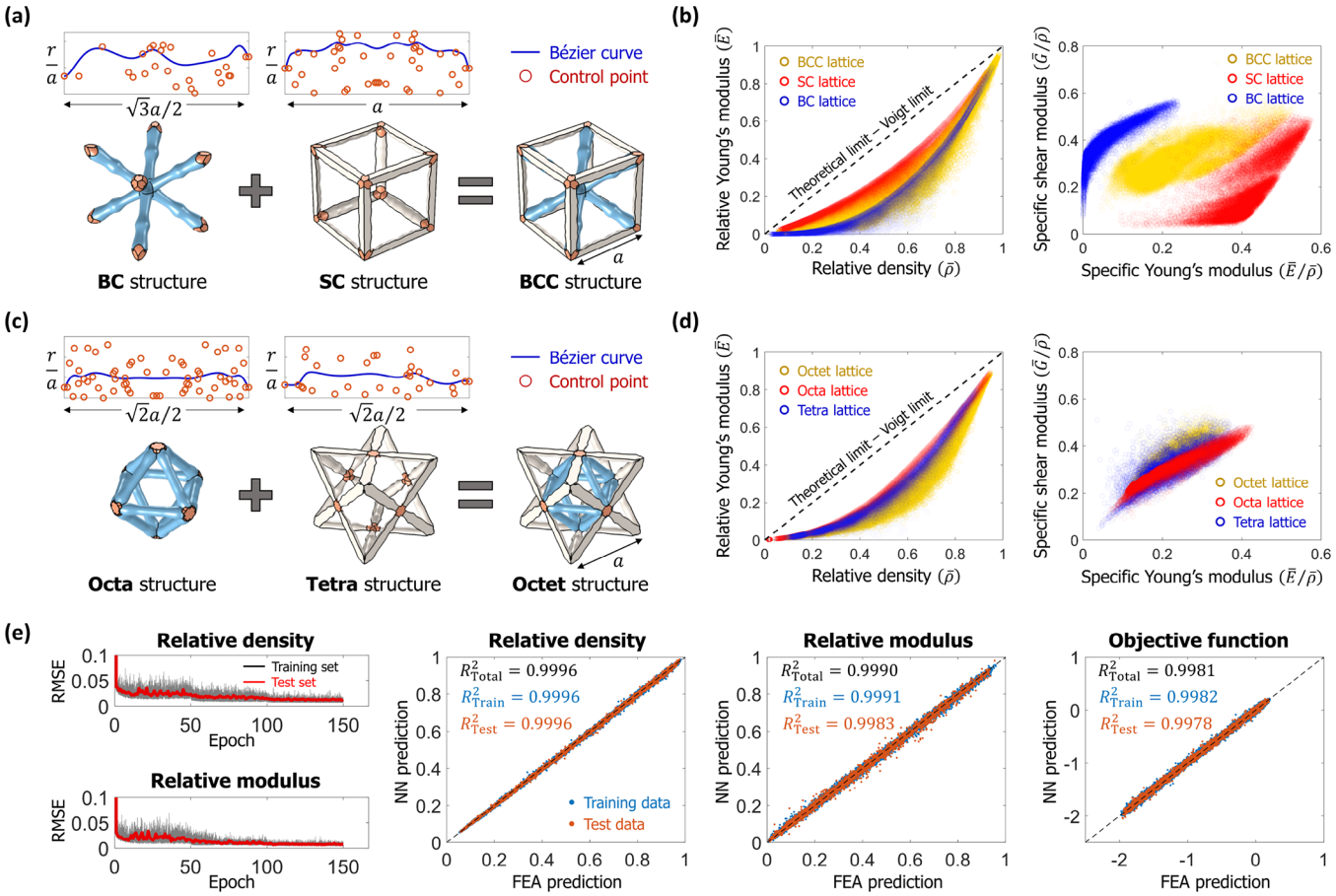

Figure 1. Bézier curves for modeling (a) body-centered (BC) and simple cubic (SC) lattice structures used in the body-centered cubic (BCC) structure and (c) octahedral (Octa) and tetrahedral (Tetra) lattice structures used in the octet-truss (Octet) structure. For BC and Tetra, a 30th-order asymmetric The Bézier curve is used and for SC and Octa lattice structures, a 60th-order symmetric Bézier curve is used. The orange sections in the schematics (a, c) represent the joining points within the BCC and Octet lattice structures. The relative Young's modulus and the specific shear modulus of the initial datasets of (b) BCC and (d) Octet group lattice structures. The dashed line in the figures is the theoretical upper limit, the Voigt limit. The relative density range for the specific shear modulus plot is $0 < \bar{\rho} < 0.4$. (e) RMSE with respect to epoch during training neural networks (NNs) for BCC. The outputs predicted by NNs are compared with the ground truth, and the R^2 is calculated by comparing the NN prediction with the ground truth. The target relative density ($\bar{\rho}_0$) for the objective function is 40%.

lattice structure, a noticeable improvement has been achieved in modulus and strength compared to a reference BC lattice consisting of cylindrical beam elements by employing graded or tapered beam elements modeled with two design parameters.[24,25] To improve the isotropy of lattice structures, multi-materials are used for the lattice, or additional tapered beam elements are inserted into the conventional lattice structure so that it can withstand loading in various directions.[3,26,27] Polycrystalline lattice structures or sandwich-type beam elements consisting of hard and soft materials have been used to enhance the toughness of the lattice structure with progressive failure.[6,28−30] However, it is widely acknowledged that tradeoffs exist among mechanical properties (such as elastic modulus and isotropy, strength and toughness, among others) where mutual improvement is difficult to achieve.[31−35] Failure to achieve comprehensive mechanical enhancement can be fatal for structural sustainability.

In this study, we present a method to enhance the elastic stiffness, strength, and toughness of lattice structures while minimizing tradeoffs by optimizing the shape of the beam elements. We reveal that enhancing the modulus by tuning the beam shape can also improve the degree of isotropy and toughness simultaneously without the sacrifice of other mechanical properties. The beam elements are modeled using a high-order Bézier curve, which offers a flexible design space and smooth surfaces in the domain. Smooth surfaces are beneficial when it comes to manufacturing, which guarantees that the structures generated from the work can be realizable for future applications. Thereafter, we employ an active learning-based design optimization approach to consider the large design space more efficiently. Our starting point is the calculation of the lattice stiffness from finite element analysis (FEA). Then, neural networks (NNs) are used for their exceptional performance in helping to probe the complicated relationship between high dimensional inputs and outputs, given the large set of design variables.[36−41] Next, genetic optimization (GO) is applied to generate new lattice designs that have superior properties compared to the initial datasets. The NNs are used to predict stiffness values faster than FEA calculations to speed up the greedy decisions during GO, which accelerates design optimization by leveraging the fast inference of the NNs. The optimized structures are fabricated using additive manufacturing. Finally, our design approach is verified through compression testing experiments and compared with the benchmark lattices consisting of cylindrical beam elements. Based on our experimental and simulation

https://doi.org/10.1021/acsami.3c02746
ACS Appl. Mater. Interfaces 2023, 15, 22543−22552

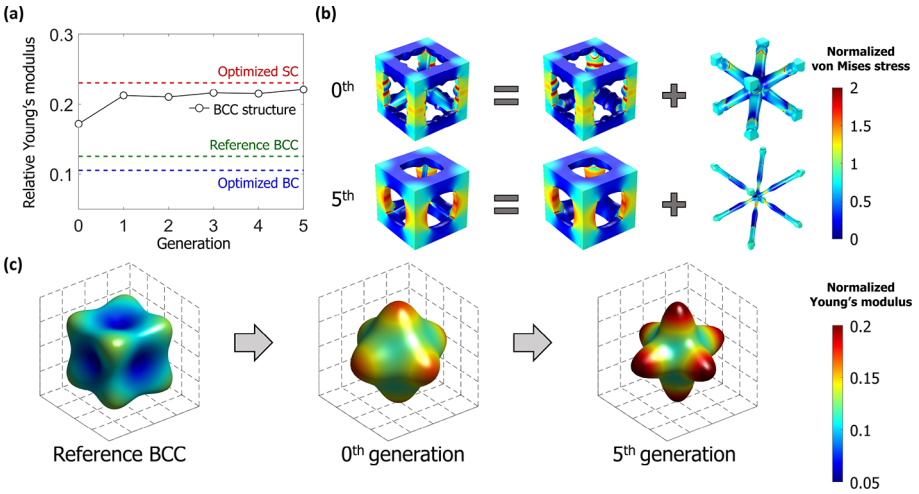

Figure 2. (a) Relative Young's modulus of body-centered cubic (BCC) structures during the optimization. The maximum modulus of each generation dataset is used for each data point in the figures. The 0th generation implies the initial datasets, and the lattice structure with a density higher than 0.4 and closest to 0.4 is chosen for the data point. (b) Normalized von Mises stress of the BCC structure at the initial and final generations under uniaxial strain loading condition. The stress is normalized by $E_0\varepsilon_0$ where E_0 is Young's modulus of base material and ε_0 is the applied strain in the z direction. (c) 3D elastic modulus plot of BCC at different generations of the optimization process.

results, we analyze the mechanisms of the high stiffness, strength, and toughness and discuss the importance of beam modeling in improving various mechanical properties of the lattice structure for next-generation high performing light-weight lattice structures.

RESULTS AND DISCUSSION

Initial Datasets of Lattice Structures. In this work, we consider a suite of lattice-type structures including simple cubic (SC), BC, body-centered cubic (BCC), octahedral (Octa), tetrahedral (Tetra), and octet-truss (Octet) lattices, which are common lattice structures studied for lightweight applications in previous studies.[2,3,6,16,20,30,42,43] Herein, lattice structures consisting of one type of beam element are referred to as "simple lattices", while "superimposed lattices" are lattice structures that have two types of beam elements (Figure 1a,c). Each superimposed lattice consists of two simple lattice structures: BCC is the superposition of SC and BC lattices, and Octet is the superposition of Octa and Tetra lattices.[43,44] A Bézier curve with a set of control points describes the shape of the beam elements, and 20,000 and 100,000 initial datasets are prepared for each simple and superimposed lattice, respectively. In order to generate initial datasets covering the entire range of relative density of lattice structure, the x, y coordinates of the control points of the Bézier curves are generated by random number generation. Each dataset includes inputs (x and y coordinates of the control points) and outputs (relative density and modulus of the lattice structure) obtained from FEA and the homogenization method described in the Computational Methods section. In order to understand the lattice-dependent mechanical properties, two elastic properties are computed including Young's modulus and shear modulus as a function of relative density, as shown in Figure 1b,d. The SC and Octa lattices have higher Young's modulus than BC and Tetra, respectively, while the opposite is true for the shear modulus, i.e., the lattice structure with a high Young's modulus has a lower shear modulus and vice versa. This is due to the activation of different deformation mechanisms depending on the loading direction for each type of lattice. For instance, under axial loading, the SC lattice shows a stretching-dominant deformation mode, whereas BC is bending-dominant (i.e., has lower bending stiffness than axial stiffness). However, under shear loading, the deformation mode of each lattice is switched, from stretching-dominant to bending-dominant.

Using the initial datasets, four different NNs (predicting relative density and modulus of BCC and Octet lattices, details in the Supporting Information: Generative machine learning-based design optimization) are trained for 150 epochs. As a result of training the four NNs, both the RMSE of the training and test datasets converge to less than 1% (Figure 1e and Figure S1). In order to verify the NNs, the relative density and Young's modulus of each lattice structure are compared with the ground truth obtained from FEA and homogenization methods. We plot the NN prediction versus the ground truth and fit the data to the line $y = x$; R^2 values close to 1 imply an accurate prediction. The output of the objective function is predicted based on the relative density and elastic modulus obtained from the NN. We obtain $R^2 = 0.9978$ and 0.9984 for the test datasets of BCC and Octet lattice, respectively, meaning that the predictions are accurate compared with the ground truth (Figure 1e and Figure S1). In terms of computational time, the NN prediction for the three-dimensional lattice structures is approximately 50 times faster than FEA. Specifically, the NN prediction takes less than 0.1 s independent of the density of the lattice structure since the NN calculates the output using the coordinates of each control point as input. Because of the fast inference and high accuracy of NNs in making the output prediction required for a greedy decision during the GO process, more new design candidates with potentially higher output can be obtained faster.

Beam-Shape Optimization for BCC and Octet Lattices. The generative deep learning algorithm, GO coupled with NNs, is applied to maximize Young's modulus of the lattice structure using the shape of the beam elements as input. The GO generates a new beam shape, and the NNs make greedy decisions to obtain new data with high mechanical properties, which accelerates the optimization process. More details on our active learning-based optimization approach are described in the Generative machine learning-based design optimization section of the Supporting Information. Young's

https://doi.org/10.1021/acsami.3c02746
ACS Appl. Mater. Interfaces 2023, 15, 22543−22552

modulus of the superimposed lattice structures is optimized by tuning the shape of the beam elements, and we investigate the effect of the beam shape on the anisotropy of the lattice structures as the optimization process progresses. The relative density is fixed at 40%, which is in the typical range of density of lattice structures used in other works.[1,3,8,20,24]

The relative modulus of the variable-beam shape BCC superimposed lattice structure gradually increases, showing a 76% improvement compared to the Reference BCC lattice consisting of cylindrical beam elements (Figure 2a). We make three interesting observations regarding the BCC superimposed lattice with respect to its constituent lattices: the SC and BC simple lattices. The modulus of the BCC lattice structures is lower than that of the optimized SC lattice at all generations during optimization. The radius of the beam element of the BC lattice in the BCC decreases as the optimization proceeds (Figure 2b). The beam element of the SC in the BCC has a smooth shape and eventually, the stress field becomes more distributed, resulting in high load-bearing performance.

In order to quantify the anisotropy of the lattice structures, the elastic modulus is calculated in all directions using coordinate transformation of the obtained fourth-order stiffness tensor and visualized with a color plot on a 3D geometry in Figure 2c.[45] In the Reference BCC structure, the modulus in the ⟨111⟩ direction (E_{111}) is larger than the modulus in the other directions, but after the optimization process, the modulus in the ⟨100⟩ direction (E_{100}) becomes stiffer than the others because the proportion of SC lattice in the Optimized BCC is larger than that of the BC lattice. This is because the SC lattice material distribution is more efficient at withstanding loading in the ⟨100⟩ direction where beam elements are parallel to the loading direction, resulting in stretching-dominant deformation.

The same design approach is applied to optimize the elastic modulus of the Octet structure studied in many previous works (Figure S2).[2,3,20,44,46] The modulus of the Octet lattice increases with the generation of GO and the modulus of the last generation shows about 35% improvement compared to the Reference Octet lattice consisting of cylindrical beams. We make two observations regarding the Octet superimposed lattice with respect to its constituent lattices: the Octa and Tetra simple lattices. The radius of the beam elements of the Tetra simple lattice decreases as generation increases. While the modulus of the Octet lattice increases with the generation of GO, it is always lower than the elastic modulus of the Optimized Octa lattice.

The Octet lattice has a similar degree of anisotropy to that of the BCC lattice as both lattices have multiple beam elements to withstand loading in various directions. The converged lattice structure has a stiffer modulus than the Reference Octet lattice in all loading directions and is more isotropic (Figure S2). The Zener ratio is calculated to estimate the degree of anisotropy of the lattices, expressed as $2c_{44}/(c_{11}-c_{12})$ where c_{ij} are the elements of the lattice structure stiffness matrix. The Zener ratio is 1 for isotropic materials and deviates from 1 when the material is anisotropic.[47] The ratio of the Reference Octet lattice is 3.05, which implies a highly anisotropic structure and it converges to 1.05 after optimization.

Based on the optimized Young's modulus of BCC and Octet lattices, we hypothesize that the optimized structure of a superimposed lattice converges to the optimized structure of one of its constituent simple lattices. To further explore this hypothesis, we discuss the simple lattice results in the next section. First, the optimized moduli of simple lattices are predicted in the entire range of the relative density. Then, a mathematical proof is introduced based on the superposition rule of the lattice structures to explain the convergence of superimposed lattices shown in the section called Convergence of Superimposed Lattice Structures.

Beam-Shape Optimization for Simple Lattices. Figures 3a and 4a show the optimized Young's modulus values of SC,

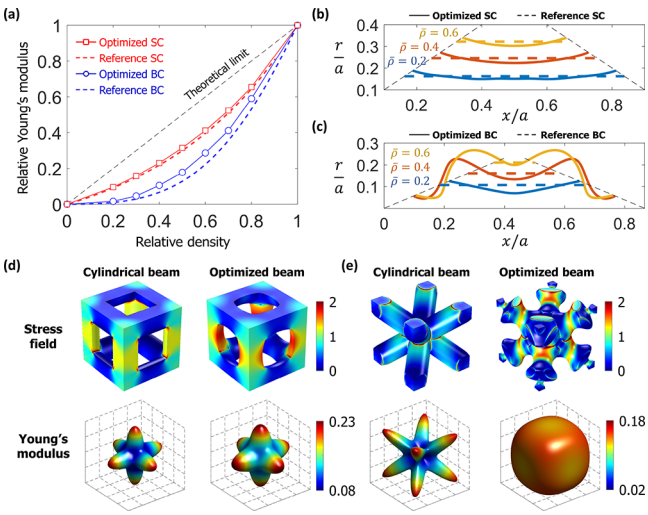

Figure 3. (a) Relative Young's modulus of simple cubic (SC) and body-centered (BC) lattice structures. The maximum modulus of each generation is used in the plots. Shape of optimized beam element in (b) SC and (c) BC lattice structures. The shape of the beam element in the reference lattice structure is a cylinder. Normalized von Mises stress field and 3D elastic modulus plot of (d) SC and (e) BC lattice structures. The relative density of lattices in (d) and (e) is 40%. For all cases, the optimized lattice structure has a more distributed stress field than its reference lattice structure counterpart at the same relative density.

BC, Octa, and Tetra lattices in the entire range of the relative density, and the results are compared with their reference lattices consisting of cylindrical beam elements with the same relative density. All optimized lattice structures have higher elastic stiffness than their reference lattice structures, as summarized in Table 1. For BC and SC lattices, the shapes of the optimized beam elements have radius variation along the beam axis and the optimized lattices have a more distributed stress field due to the smooth geometries of the optimized beam elements, whereas the reference lattice structures have high stress concentration at joints, where the beam elements intersect (Figure 3b–e and Figure S3). In the optimized structures, more materials are shifted toward each joint to effectively strengthen the joints and alleviate the stress concentration. Due to the crystallographic symmetry of the lattices, when both BC and SC lattices have optimized modulus, they have symmetric beam element shapes, e.g., [111] is the same as $[\bar{1}\bar{1}\bar{1}]$ for the BC lattice and [100] is the same as $[\bar{1}00]$ for the SC lattice. The optimized beam element of the BC lattice has a local minimum radius along the beam axis, and the number of the local minimum radii increases with the relative density, effectively reducing the stress concentration and increasing the modulus of the lattice. The Optimized SC has a higher elastic modulus than the Optimized BC for all relative densities and has a more distributed stress

https://doi.org/10.1021/acsami.3c02746
ACS Appl. Mater. Interfaces 2023, 15, 22543−22552

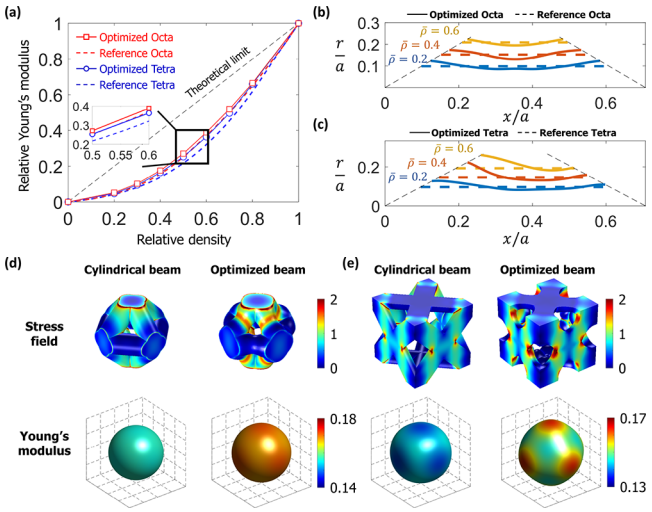

Figure 4. (a) Relative Young's modulus of octahedral (Octa) and tetrahedral (Tetra) lattice structures. The shape of optimized beam element in (b) Octa and (c) Tetra lattice structures. The shape of beam element in the reference lattice structure is a cylinder. Normalized von Mises stress field and 3D elastic modulus plot of (d) Octa and (e) Tetra lattice structures. The relative density of lattices in (d) and (e) is 40%. For all cases, the optimized lattice structure has a more distributed stress field than its reference lattice structure counterpart at the same relative density.

field. From a structural point of view, most of the beam elements in the SC lattice are aligned with the loading direction, which results in stretching-dominant deformation, whereas the BC lattice shows bending-dominant deformation under loading in the ⟨100⟩ direction. Since the stress field by stretching-dominant deformation is uniform, SC has a more simplified beam shape than BC, which has local minimum points in the optimized Bézier curves. Hence, the BC lattice is less efficient than SC in terms of load bearing, and thus, it has a lower modulus. In particular, the shape of the Optimized SC at a density of 40% is similar to the SC lattice in BCC at the sixth (final) generation.

Results show that the elastic modulus of the Optimized SC lattice is stiffer than that of the Reference SC lattice in all directions. To observe the degree of anisotropy depending on the change in E_{100}, the Zener ratio of the Reference and the Optimized SC lattice is calculated (Table 1). The Zener ratio, the degree of anisotropy, can also be interpreted as the ratio of E_{111} to E_{100}, i.e., E_{111}/E_{100}, i.e., Zener ratio of isotropic materials is 1.[48] All SC lattices have a ratio less than 1 because E_{100} is stiffer than E_{111}, owing to the stretching-dominant deformation mode in the ⟨100⟩ direction of the SC lattice. The Zener ratio of the Optimized SC is larger than that of the Reference SC of the same density and approaches a value of 1 after optimization. That is, through optimization of the beam shape, the modulus increases in all directions, and at the same time, it becomes less anisotropic. These improvements are attributed to the distributed stress field obtained from the optimized beam elements. In the case of a sharp joint, high stress is applied to the joint part and the intensity of the stress concentration is sensitive to the direction of the applied loading, and thus the elastic modulus changes significantly due to the loading direction. Consequently, the smooth joint of the Optimized SC results in a modulus insensitive to the change in loading direction compared to the Reference SC, and thus, possesses higher isotropy. On the other hand, in the case of the BC lattice structure, E_{111} is larger than E_{100} because the beam elements are aligned in the ⟨111⟩ direction, having stretching-dominant deformation under ⟨111⟩ loading, and therefore, the Zener ratio of BC is greater than 1. Optimizing E_{100}, decreases E_{111}, and as a result, the Zener ratio is reduced and becomes more isotropic than the Reference BC, i.e., both E_{100} and E_{111} get closer as the optimization process progresses.

The Optimized Octa lattice has a higher elastic modulus at all relative densities than the Optimized Tetra lattice, but the difference is not significant compared to the SC-BC case, which is less than 11% for all results (Figure 4 and S4). This similarity is believed to be due to their identical beam inclination angle with respect to loading direction (45 degrees), resulting in similar deformation modes. However, horizontal beams on the $z = a/2$ plane of the Octa lattice more effectively constrain the horizontal expansion during compressive loading than the horizontal beams at the top and bottom of the Tetra lattice, and therefore slightly stiffens the overall modulus of the Octa lattice. Tetra has a higher stress concentration than the Octa lattice due to sharper corners at the interface created by the intersection of two beam elements (Octa: 34.9°, Tetra: 29.2°), which results in more bending stress with a lower modulus (Figure S5). Interestingly, the optimized beam element of Tetra has an asymmetric shape unlike SC, BC, and Octa structures (Figure 4b and c). From a crystallographic perspective, the positive direction of the beam axis in Tetra is different from its negative direction whereas the two directions are indistinguishable in the other simple lattices. Due to the unbalanced architecture of Tetra, there are two different types of joints and the joints near the lattice vertices have less volume than joints near the center of the lattice face

Table 1. Relative Young's Modulus ($\bar{E}$) and Zener Ratio (Z) of the Lattice Structures

	$\bar{\rho}$ = 0.2		$\bar{\rho}$ = 0.4		$\bar{\rho}$ = 0.6	
	$\bar{E}$	Z	$\bar{E}$	Z	$\bar{E}$	Z
reference BCC	0.04283	1.4088	0.12560	2.5545	0.28137	1.1604
reference BC	0.00983	10.2369	0.06575	9.0128	0.22087	1.6332
optimized BC	0.01630	5.4260	0.10528	1.2089	0.28653	0.7753
reference SC	0.09082	0.1268	0.21817	0.3424	0.39485	0.6026
optimized SC	0.09528	0.1721	0.23069	0.4298	0.41170	0.6670
reference Octet	0.03794	1.7405	0.11483	3.0491	0.26419	1.3174
reference Tetra	0.04203	1.4204	0.13718	1.0648	0.31890	0.8863
optimized Tetra	0.04683	1.2538	0.16384	0.8738	0.36390	0.7350
reference Octa	0.04496	1.3900	0.15549	1.0090	0.36822	0.8439
optimized Octa	0.05194	1.3208	0.17541	0.9755	0.38917	0.8423

https://doi.org/10.1021/acsami.3c02746
ACS Appl. Mater. Interfaces 2023, 15, 22543−22552

(Figure S6). Therefore, in the Optimized Tetra, the beam radius near the origin (vertices of the lattice) is thicker than near the end of the beam (center of the lattice face) to obtain more balanced loading on joint parts compared to the Reference Tetra lattice. In summary, the moduli of Octa and Tetra are similar because the two optimized structures have similar deformation modes, but the Octa lattice has a higher elastic modulus because of lower stress concentration and more balanced structure than the Tetra lattice.

Maximizing E_{100} of the Octa lattice increases E_{111} because some beam elements not on the $z = a/2$ contribute to load bearing under [111] loading, and as a result, the Zener ratio changes less than in other lattice structures. Hence, by optimizing the beam shape of the Octa structure, the modulus is improved in all directions without loss or sacrifice of the degree of isotropy. Interestingly, the Octa lattice with 40% density shows a transition of the maximum modulus from E_{111} to E_{100} during optimization, whereas the Reference Octa lattice with relative densities of 20 or 40% has a larger E_{111} than E_{100} (Figure 4d and Figure S4). In the case of the Reference Octa lattice at 40% density, E_{100} and E_{111} are similar, and it is nearly isotropic having a Zener ratio close to 1. Since E_{100} is maximized through optimization, E_{100} becomes larger than E_{111}.

When E_{100} is maximized by optimizing the beam shape of the Tetra lattice, E_{111} does not change significantly after the optimization and the Zener ratio decreases as E_{100} increases. At a density of 40%, E_{100} becomes stiffer than E_{111} as optimization progresses and the Zener ratio of the Optimized Tetra drops below 1. That is, in the case of Octa and Tetra structures, the degree of anisotropy and elastic modulus are improved simultaneously through beam shape optimization up to a relative density of 40%. In general, the lattice structure has a very high or small Zener ratio deviating from 1 at a low density because it has a stiffer modulus in the beam axis direction, resulting in a highly anisotropic modulus. As the density increases, the lattice efficiently withstands loading in various directions because more materials are spatially distributed in the lattice structure space, and therefore the Zener ratio gets closer to 1. On the other hand, when the density is too high, the Octa and Tetra lattices are almost enclosed by the beam elements due to a large overlapping between each beam element, creating an almost closed-cell foam structure. Many studies utilize lattice structures in the low-density region below 40% for open cell structures, and it is believed that our method can be utilized in various existing lattice structure applications since most of the simple lattice structures studied in our work show improvement in both elastic modulus and isotropy at moderate density (<40%).

Convergence of Superimposed Lattice Structures. Next, the convergence of the modulus of BCC and Octet lattices to that of SC and Octa, respectively, is proved by introducing a simple mathematical model. First, the superposition rule is employed based on the linear elasticity assumption of our problem. When the relative elastic modulus of a superimposed lattice C is $\bar{E}_C$ and the lattice constant is a, the modulus of lattice C consisting of simple lattices A and B can be obtained from force equilibrium as expressed in eq 1

$$\bar{E}_C = \bar{E}_A + \bar{E}_B \tag{1}$$

This is different from the conventional rule of mixtures used for predicting the effective properties of composites because the lattices A, B, and C have the same lattice volume a^3, whereas the total volume increases in the rule of mixtures by adding new phases (Figure S7). Therefore, when the relative density of lattice structure C is $\bar{\rho}$ and lattice A in the C structure has a relative density of $\bar{\rho}_1$, the modulus of C can be expressed as

$$\bar{E}_C(\bar{\rho}) = \bar{E}_A(\bar{\rho}_1) + \bar{E}_B(\bar{\rho} - \bar{\rho}_1) \tag{2}$$

Since the elastic modulus of each lattice is lower than that of its optimized structure, eq 2 can be expressed as

$$\bar{E}_C(\bar{\rho}) \le \bar{E}_A^{\max}(\bar{\rho}_1) + E_B^{\max}(\bar{\rho} - \bar{\rho}_1) \tag{3}$$

If lattice A is stiffer than lattice B under the same relative density, eq 3 is then further simplified by using the fact that $\bar{E}_B^{\max}(\bar{\rho} - \bar{\rho}_1) < \bar{E}_A^{\max}(\bar{\rho} - \bar{\rho}_1)$:

$$\bar{E}_C(\bar{\rho}) \le \bar{E}_A^{\max}(\bar{\rho}_1) + \bar{E}_A^{\max}(\bar{\rho} - \bar{\rho}_1) \tag{4}$$

Next, the Gibson–Ashby power law is employed, which is commonly used as an empirical model for describing the relationship between the mechanical property and density of lattice structures.[49−52] The power law for the relative modulus is expressed as $\bar{E} = K\bar{\rho}^n$ where K and n are coefficients depending on the lattice structures and our optimized results are fitted to the law using $K = 1$, satisfying $\bar{E} = 1$ when $\bar{\rho} = 1$, i.e., a single parameter n is used for the curve fitting. As a result, all R^2 values are higher than 99.5%, which shows the good predictive capability of the law (Figure S8). Since it always satisfies $(\bar{\rho}_1)^n + (\bar{\rho} - \bar{\rho}_1)^n \le (\bar{\rho})^n$ for positive n, eq 4 can finally be expressed as $\bar{E}_C(\bar{\rho}) \le \bar{E}_A^{\max}(\bar{\rho})$, which proves that the elastic modulus of the superimposed lattices such as BCC and Octet are strictly upper bounded by their corresponding optimized simple lattices SC and Octa. Therefore, if the optimization is performed using the Bézier curve made without minimum radius constraint, then the size of the BC and Tetra parts in BCC and Octet, respectively, would become infinitesimally small and eventually disappear. Our proof can be expanded to more general lattices consisting of two or more simple lattices, and the optimized structure of the superimposed lattice converges to the optimized structure of the simple lattice, which is the stiffest among the components of the superimposed lattice.

We plot the Ashby chart with the Gibson–Ashby power law $\bar{E} = \bar{\rho}^n$ $(0 \le \bar{\rho} \le 1)$ for each optimized simple lattice and reference superimposed lattice (Figure S8). In the case of the Voigt limit, n is 1, which represents an ideal case, and as the value of n increases, the modulus decreases significantly with increasing density. Hence, a lattice structure with a lower n has a higher specific modulus. For example, in the case of Al_2O_3, which has been widely used as a base material for lattice structures in previous studies, the density of the base material is 4.0 g/cm^3 and the modulus of elasticity is 375 GPa.[6,42,50,53,54] When Al_2O_3 is used as the base material, the moduli of the lattice structures such as Optimized BC, BCC, and Octet are in the regime of conventional foam materials in the Ashby chart, but our Optimized Octa, Tetra, and SC are located in a higher area than conventional materials, toward the region of higher specific modulus.

Similarly, optimization is conducted to find the minimum modulus of the SC and BC lattices. To predict the minimum modulus, the objective function is minimized using a penalty coefficient k, which represents the sensitivity of the density constraint to the objective function. Here, Young's modulus is minimized using $k = 5$.[17] As the optimization proceeds, the

https://doi.org/10.1021/acsami.3c02746
ACS Appl. Mater. Interfaces 2023, 15, 22543−22552

cross-sectional area near the vertices of the unit cell becomes very small, and a very high stress concentration arises due to the small cross section (Figure S9). If the radius constraint is not used when modeling the Bézier curve, then the modulus converges to zero because a sufficiently small cross-sectional area is expected at the vertex of the unit lattice, which gives rise to a stress singularity. Therefore, based on the superposition rule, the theoretical lower bound of a superimposed lattice is 0, which can be explained by the Hashin−Shtrikman lower bound for elastic material with cubic symmetry.[55]

Experimental Validation of the Beam Shape Optimization. In this work, generative machine learning-based design optimization is applied for simulation data only because it would take a lot of time and cost when constructing training data using only experimental data. Optimized lattice structures with a relative density of 40% are fabricated using additive manufacturing to verify our design approach (Figure 5). The

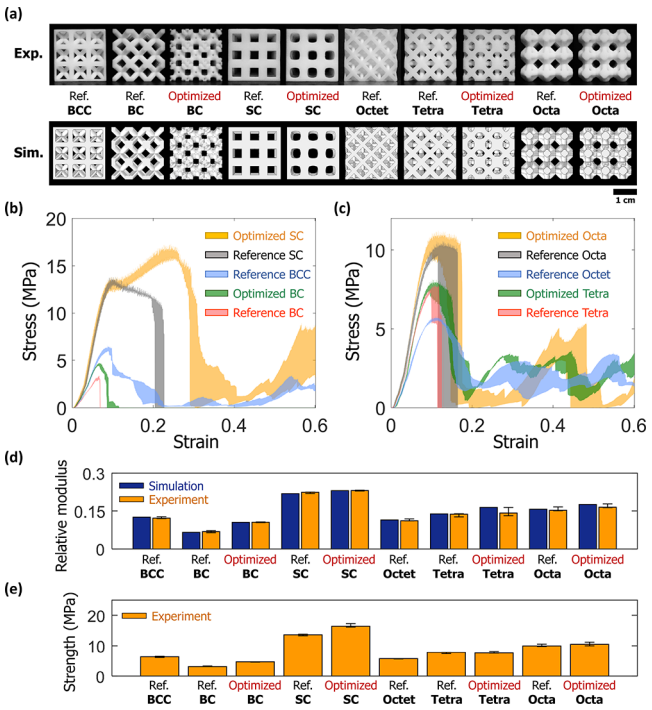

Figure 5. (a) Reference (Ref.) and optimized lattice structures fabricated by additive manufacturing (Exp.) and modeled by simulation (Sim.). Stress−strain curves of the (b) BCC and (c) Octet group. (d) Relative Young's modulus and (e) strength measured from compression testing. Three samples are tested for each case to show the reproducibility of our experiments, and error bars show the variance.

elastic moduli are measured from the elastic regime of the stress−strain curve obtained from experiment and they show good agreement with simulation results. Moreover, the strength of the lattice structure shows a similar trend to the elastic modulus because the optimized structures have distributed stress fields leading to a high modulus at a fixed density, resulting in low stress concentration. Hence, structures with high modulus also have high strength due to distributed stress fields under the same loading conditions.

All optimized lattice structures show more progressive failure with a large strain limit compared to their reference lattice structures (Figure 6). Remarkable improvement is observed for SC and Tetra lattices. The Reference SC lattice shows catastrophic fracture, which is undesirable for engineering applications. On the other hand, our Optimized SC lattice shows hardening behavior, starting with the onset of buckling and results in a gradual fracture behavior after reaching maximum stress (Supporting Information, Videos 1 and 2). Similarly, the Optimized Tetra structure reveals progressive failure, and the toughness is remarkably improved compared to its reference lattice even though it is made of brittle resin (Figure 6 and Supporting Information, Videos 3 and 4). The mechanism of the high toughness is believed to originate from the distributed stress field of the optimized lattices, especially near joints, where beams intersect. The optimized beam element has a smooth shape with radius variation along the beam axis and obtains a distributed stress field, as explained by our simulation results. Due to the low peak stress, the optimized structure has low strain energy near joints and a small amount of energy is released as surface energy and kinetic energy when the crack nucleates (Figure 6b,d). Meanwhile, the high strain energy is stored near the tip of reference lattices, which results in high surface energy and high kinetic energy release after crack nucleation. Hence, the fracture of the reference lattices is more brittle than their optimized counterparts, showing low toughness and a small strain limit. This mechanism can be applied only for lattice structures made of brittle materials under a mechanical loading in the ⟨100⟩ direction. The stress−strain curve of our experimental results is different from the typical stress−strain curve for the porous material, which has been observed in many papers.[56,57] One of the major reasons for this discrepancy is due to the material type. When the base material is ductile, the lattice structure undergoes more deformation without fracture, displaying linear deformation, plateau, and densification, whereas the lattice structure made of brittle materials fails before the structure is densified. Hence, our stress−strain behavior is closer to a material failure rather than densification curve.

To help understand the simultaneous improvement in modulus and toughness, we make a rough estimate of the ultimate stress/strain by comparing the maximum von Mises stress of the lattices and a failure threshold (normalized strength, $\sigma_y/E_0 = 1$) under uniaxial loading. Figure S10 depicts the simulated full stress−strain curve of reference and optimized lattice structures. In all cases, we observe that the maximum von Mises stress of the optimized lattices (solid curves) reaches the failure threshold at a larger applied strain compared to their respective reference lattices (dashed curves), in agreement with experimental results. Based on linear elasticity, we can further conclude that the maximum von Mises stress is reduced by around 30% for SC, Octa, and BC lattices compared to their references under the same applied strain. It is noted that the linear material model used here is a rough approximation, while a nonlinear material damage model is required to obtain more accurate numerical estimates of lattice strength and toughness.

CONCLUSIONS

The optimized shapes of beam elements of various lattice structures are presented using a generative deep learning-based design optimization. A high-order Bézier curve is adopted to describe the shape of the beam elements with high design flexibility, and NNs are trained to understand the complicated relationship between high-dimensional design input and relative Young's modulus and density of the lattices. The

https://doi.org/10.1021/acsami.3c02746
ACS Appl. Mater. Interfaces 2023, 15, 22543−22552

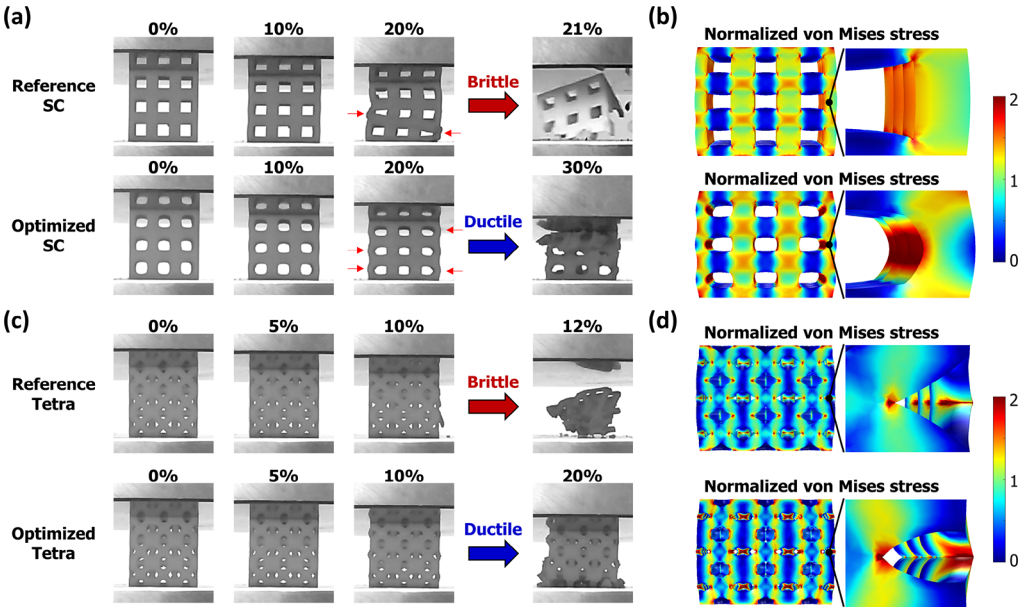

Figure 6. Images from experiments with optimized (a) simple cubic (SC) and (c) tetrahedral (Tetra) lattice structures at different levels of applied strain. Thin red arrows in the images indicate buckled beam elements. The optimized lattice structures show more progressive failure (Ductile) compared to their reference lattice structures, which show catastrophic failure (Brittle). (b) SC and (d) Tetra lattice structures (color images show the normalized von Mises stress field). Optimized structures have more distributed stress fields.

NNs work to predict modulus and density faster than FEA and homogenization methods when making greedy decisions during GO for design acceleration. The new datasets generated by GO have higher mechanical properties than the initial datasets. The 3D Young's modulus plot and the Zener ratio are calculated to explain the beam shape-dependent anisotropy of the lattice structures. Our optimized lattice structures possess superior stiffness (+59%), strength (+49%), toughness (+106%), and isotropy (+645%) compared to benchmark lattices consisting of cylindrical beams. It is believed that this comprehensive enhancement benefits from the optimized lattice beam shapes, which distribute the loading over the entire lattice structure. Our NN-assisted GO generative machine learning-based beam shape design provides opportunities to improve the mechanical properties of lattice structures, evading the tradeoff dilemmas between properties.

EXPERIMENTAL METHODS

Stereolithography (SLA) is employed for precise three-dimensional fabrication with a layer resolution of 50 μm, which is three orders of magnitude less than the lattice constant of 1 cm used in our experiments. The 3D printer used in this work is the Form 3 developed by Formlabs, and the base material is white standard light-reactive resin. The SLA fabricates the lattice structures by selectively curing the resin layer by layer using an ultraviolet laser beam. For a baseline comparison, reference lattice structures having a cylinder beam element are also fabricated for each case and compression experiments are performed. Three different samples are prepared for each lattice to estimate the fabrication accuracy and reproducibility. In compression testing, the fabricated lattice structures are subjected to uniaxial compression using an Instron 5900-series universal testing system. After placing the samples between two steel plates, the mechanical load is applied to the specimen with a quasi-static displacement control of 2 mm/min at a strain rate of about 10^{-3}/s (Supporting information, Videos 1–4).

COMPUTATIONAL METHODS

The Octet and BCC structures are modeled using high-order Bézier curves. Each of the two superimposed lattice structures consists of two simple lattice structures: BCC is the superposition of SC and BC structures, and the Octet structure is the superposition of Octa and Tetra structures (Figure 1). The Bézier curve is a parametric curve with respect to the parameter t and is described by the control point sets, expressed by the following equation:

$$\boldsymbol{B}(t) = \sum_{k=0}^{m} \left[\binom{m}{k} (1-t)^{m-k} t^{k} \boldsymbol{P}_k \right], \quad 0 \le t \le 1 \tag{5}$$

where $\boldsymbol{P}_k$ is the kth control point and m is the order of the Bézier curve, i.e., $m + 1$ control points are used for modeling. Since our focus is Young's modulus, which is governed by linear elasticity, all lengths are normalized by the lattice constant (a) of the lattice structure to suggest a scale-free design. The x coordinates of the first and last control points are fixed at 0 and L, respectively, to model a beam of length L. For modeling the beam element in BC and Tetra, a 30th-order Bezier curve is adopted, so a total of 31 control points are used. In the case of SC and Octa, the shape of the beam must be symmetric to satisfy the cubic symmetry condition of the lattice structures. Hence, the beam elements in the two lattice structures are described by 60th-order symmetric Bézier curves with the same number of control points as BC and Tetra. To create a symmetric curve of length L, the x coordinate of $\boldsymbol{P}_{30}$ is fixed at $L/2$, and $\boldsymbol{P}_{31}$–$\boldsymbol{P}_{60}$ are obtained by symmetrizing $\boldsymbol{P}_0$–$\boldsymbol{P}_{29}$ with respect to $x = L/2$. Therefore, a total of 60 independent features are used in each nonsymmetric and symmetric 60th-order Bézier curve, and a total of 120 independent inputs are used to model the shape of the beam elements in the BCC and Octet structures. The coordinates of independent control points are determined through random number generation to create initial datasets, and the Bézier curves revolve with respect to the beam axis to create 3D beam elements. We set a minimum radius of the Bézier curve equal to $0.01a$ to avoid numerical or manufacturing problems during FEA and 3D printing.

FEA and the homogenization method are employed to calculate the stiffness of the lattice structure. A commercial code, COMSOL Multiphysics,[58] is used for the FEA, and the material properties used in our simulations are $E_0 = 1$ (dimensionless unit) and $\nu = 0.33$. In this study, a linear elastic material model is adopted because

https://doi.org/10.1021/acsami.3c02746
ACS Appl. Mater. Interfaces 2023, 15, 22543–22552

infinitesimal deformation theory is used to calculate the elastic response of the lattice structures. Hence, our approach is valid for predicting elastic properties and geometric or material nonlinearity should be considered to predict effective nonlinear properties of the lattice structure. The lattice structures are meshed using three-dimensional linear tetrahedral elements, a displacement of $-0.01a$ is applied downward to the upper surface of the unit cell, and a periodic boundary condition is applied to all other surfaces of the unit cell to describe an infinitely periodic lattice structure. For shear loading, periodic and displacement boundary conditions are applied to all the outer surfaces of the lattice to make a homogeneously tilted lattice. The boundary conditions for two loading modes (axial compression and shear) are listed in Table S1. The homogenization method is then applied to calculate the macroscopic stress applied to the lattice structure using the stress field obtained from FEA. If the lattice structure is viewed as a composite composed of void (matrix) and reinforcement (beam elements), then the macroscopic stress applied to this composite can be expressed as

$$\bar{\boldsymbol{\sigma}} = f_0 \bar{\boldsymbol{\sigma}}_0 + f_1 \bar{\boldsymbol{\sigma}}_1 \tag{6}$$

where f_i is volume fraction and $\bar{\boldsymbol{\sigma}}_i$ is the volume-averaged stress of each phase (0: void, 1: lattice structure).[59] Equation 6 of the homogenization method to predict the volume-averaged stress of the composite is valid for any nonlinear material models. Since the stress applied to the void is 0 and the volume fraction of the lattice structure is the same as the relative density ($\bar{\rho} = \rho_{\text{lattice}}/\rho_{\text{base material}}$), it can be further simplified as

$$\bar{\boldsymbol{\sigma}} = \bar{\rho}\, \bar{\boldsymbol{\sigma}}_1 \tag{7}$$

According to the boundary conditions, the only nonzero macroscopic strain component is ε_{zz} for compression and γ_{xz} for shear. Finally, the stiffness tensor $\mathbf{C}$ of the lattice structure is calculated using macroscopic stress and strain and Hooke's law expressed as

$$\bar{\boldsymbol{\sigma}} = \mathbf{C} : \bar{\boldsymbol{\varepsilon}} \tag{8}$$

where : represents double contraction.

■ ASSOCIATED CONTENT

Supporting Information

The Supporting Information is available free of charge at https://pubs.acs.org/doi/10.1021/acsami.3c02746.

Compression testing video of the Reference SC (MP4)
Compression testing video of the Optimal SC (MP4)
Compression testing video of the Reference Tetra (MP4)
Compression testing video of the Optimal Tetra (MP4)
Generative machine learning-based design optimization, boundary condition for FEA, cross section plots of optimized Octa and Tetra lattices, joint parts in Tetra, schematic of the rule of mixture, Gibson–Ashby law for lattice structures, minimized Young's modulus of SC and BC lattices, architecture of the neural networks, work flow chart of the design optimization, and stress–strain relationships of lattice structures predicted from FEA (PDF)

■ AUTHOR INFORMATION

Corresponding Author

Grace X. Gu − *Department of Mechanical Engineering, University of California, Berkeley, California 94720, United States;* orcid.org/0000-0001-7118-3228; Email: ggu@berkeley.edu

Authors

Sangryun Lee − *Department of Mechanical Engineering, University of California, Berkeley, California 94720, United States;* Present Address: Division of Mechanical and Biomedical Engineering, Ewha Womans University, Seoul 03760, Republic of Korea (S.L.)

Zhizhou Zhang − *Department of Mechanical Engineering, University of California, Berkeley, California 94720, United States*

Complete contact information is available at: https://pubs.acs.org/10.1021/acsami.3c02746

Notes

The authors declare no competing financial interest.

■ ACKNOWLEDGMENTS

This research was supported by the Basic Science Research Program through the National Research Foundation of Korea (NRF) funded by the Ministry of Education (fund number: 2020R1A6A3A03039104), ASME Haythornthwaite Foundation Research Initiation Grant, Office of Naval Research (fund number: N00014-21-1-2604), and National Science Foundation (fund number: DMREF-2119276).

■ REFERENCES

(1) Chen, W.; Watts, S.; Jackson, J. A.; Smith, W. L.; Tortorelli, D. A.; Spadaccini, C. M. Stiff Isotropic Lattices Beyond the Maxwell Criterion. *Sci. Adv.* **2019**, *5*, No. eaaw1937.

(2) Xu, S. Q.; Shen, J. H.; Zhou, S. W.; Huang, X. D.; Xie, Y. M. Design of Lattice Structures with controlled anisotropy. *Mater. Design* **2016**, *93*, 443–447.

(3) Feng, J. W.; Liu, B.; Lin, Z. W.; Fu, J. Z. Isotropic Octet-Truss Lattice Structure Design and Anisotropy Control Strategies for Implant Application. *Mater. Design* **2021**, *203*, No. 109595.

(4) Meza, L. R.; Zelhofer, A. J.; Clarke, N.; Mateos, A. J.; Kochmann, D. M.; Greer, J. R. Resilient 3D hierarchical architected metamaterials. *Proc. Natl. Acad. Sci.* **2015**, *112*, 11502–11507.

(5) Bauer, J.; Schroer, A.; Schwaiger, R.; Kraft, O. Approaching Theoretical Strength in Glassy Carbon Nanolattices. *Nat. Mater.* **2016**, *15*, 438–443.

(6) Bauer, J.; Hengsbach, S.; Tesari, I.; Schwaiger, R.; Kraft, O. High-Strength Cellular Ceramic Composites with 3D Microarchitecture. *Proc. Natl. Acad. Sci.* **2014**, *111*, 2453–2458.

(7) Zadpoor, A. A. Additively Manufactured Porous Metallic Biomaterials. *J. Mater. Chem. B* **2019**, *7*, 4088–4117.

(8) Burton, H. E.; Eisenstein, N. M.; Lawless, B. M.; Jamshidi, P.; Segarra, M. A.; Addison, O.; Shepherd, D. E. T.; Attallah, M. M.; Grover, L. M.; Cox, S. C. The Design of Additively Manufactured Lattices to Increase the Functionality of Medical Implants. *Mater. Sci. Eng. C* **2019**, *94*, 901–908.

(9) Vasiliev, V. V.; Razin, A. F. Anisogrid Composite Lattice Structures for Spacecraft and Aircraft Applications. *Compos. Struct.* **2006**, *76*, 182–189.

(10) Wang, C. Y.; Li, Y.; Zhao, W. Z.; Zou, S. C.; Zhou, G.; Wang, Y. L. Structure Design and Multi-Objective Optimization of a Novel Crash Box Based on Biomimetic Structure. *Int. J. Mech. Sci.* **2018**, *138*, 489–501.

(11) Yin, S.; Chen, H. Y.; Wu, Y. B.; Li, Y. B.; Xu, J. Introducing Composite Lattice Core Sandwich Structure as an Alternative Proposal for Engine Hood. *Compos. Struct.* **2018**, *201*, 131–140.

(12) Dong, G. Y.; Tang, Y. L.; Li, D. W.; Zhao, Y. Y. F. Design and Optimization of Solid Lattice Hybrid Structures Fabricated by Additive Manufacturing. *Addit. Manuf.* **2020**, *33*, No. 101116.

(13) Spadoni, A.; Ruzzene, M. Numerical and Experimental Analysis of the Static Compliance of Chiral Truss-Core Airfoils. *J. Mech. Mater. Struct.* **2007**, *2*, 965–981.

(14) Vasiliev, V. V.; Barynin, V. A.; Razin, A. F. Anisogrid Composite Lattice Structures - Development and Aerospace Applications. *Compos. Struct.* **2012**, *94*, 1117–1127.

(15) Matlack, K. H.; Bauhofer, A.; Krodel, S.; Palermo, A.; Daraio, C. Composite 3D-Printed Metastructures for Low-Frequency and Broadband Vibration Absorption. *Proc. Natl. Acad. Sci.* **2016**, *113*, 8386−8390.
(16) Egan, P. F.; Gonella, V. C.; Engensperger, M.; Ferguson, S. J.; Shea, K. Computationally Designed Lattices with Tuned Properties for Tissue Engineering Using 3D Printing. *PLoS One* **2017**, *12*, 1−20.
(17) Lee, S.; Zhang, Z. Z.; Gu, G. X. Generative Machine Learning Algorithm for Lattice Structures with Superior Mechanical Properties. *Mater. Horiz.* **2022**, *9*, 952−960.
(18) Crook, C.; Bauer, J.; Izard, A. G.; de Oliveira, C. S.; Silva, J. M. D. E.; Berger, J. B.; Valdevit, L. Plate-Nanolattices at the Theoretical Limit of Stiffness and Strength. *Nat. Commun.* **2020**, *11*, 1579.
(19) Liu, Y. B. Mechanical Properties of a New Type of Plate-Lattice Structures. *Int. J. Mech. Sci.* **2021**, *192*, No. 106141.
(20) Tancogne-Dejean, T.; Mohr, D. Elastically-Isotropic Truss Lattice Materials of Reduced Plastic Anisotropy. *Int. J. Solids Struct.* **2018**, *138*, 24−39.
(21) Khaleghi, S.; Dehnavi, F. N.; Baghani, M.; Safdari, M.; Wang, K.; Baniassadi, M. On the Directional Elastic Modulus of the TPMS Structures and a Novel Hybridization Method to Control Anisotropy. *Mater. Design* **2021**, *210*, No. 110074.
(22) Munford, M.; Hossain, U.; Ghouse, S.; Jeffers, J. R. T. Prediction of Anisotropic Mechanical Properties for Lattice Structures. *Addit. Manuf.* **2020**, *32*, No. 101041.
(23) Andrew, J. J.; Schneider, J.; Ubaid, J.; Velmurugan, R.; Gupta, N. K.; Kumar, S. Energy Absorption Characteristics of Additively Manufactured Plate-Lattices Under Low-Velocity Impact Loading. *Int. J. Impact Eng.* **2021**, *149*, No. 103768.
(24) Tancogne-Dejean, T.; Mohr, D. Stiffness and Specific Energy Absorption of Additively-Manufactured Metallic BCC Metamaterials Composed of Tapered Beams. *Int. J. Mech. Sci.* **2018**, *141*, 101−116.
(25) Bai, L.; Yi, C. Y.; Chen, X. H.; Sun, Y. X.; Zhang, J. F. Effective Design of the Graded Strut of BCC Lattice Structure for Improving Mechanical Properties. *Materials* **2019**, *12*, 2192.
(26) Altamimi, S.; Lee, D. W.; Barsoum, I.; Rowshan, R.; Jasiuk, I. M.; Abu Al-Rub, R. K. On Stiffness, Strength, Anisotropy, and Buckling of 30 Strut-Based Lattices with Cubic Crystal Structures. *Adv. Eng. Mater.* **2022**, *24*, 2101379.
(27) Latture, R. M.; Begley, M. R.; Zok, F. W. Design and Mechanical Properties of Elastically Isotropic Trusses. *J. Mater. Res.* **2018**, *33*, 249−263.
(28) Yavas, D.; Liu, Q. Y.; Zhang, Z. Y.; Wu, D. Z. Design and Fabrication of Architected Multi-Material Lattices with Tunable Stiffness, Strength, and Energy Absorption. *Mater. Design* **2022**, *217*, No. 110613.
(29) Pham, M. S.; Liu, C.; Todd, I.; Lertthanasarn, J. Damage-Tolerant Architected Materials Inspired by Crystal Microstructure. *Nature* **2019**, *565*, 305−311.
(30) Meza, L. R.; Greer, J. R. Mechanical Characterization of Hollow Ceramic Nanolattices. *J. Mater. Sci.* **2014**, *49*, 2496−2508.
(31) Wei, Y. J.; Li, Y. Q.; Zhu, L. C.; Liu, Y.; Lei, X. Q.; Wang, G.; Wu, Y. X.; Mi, Z. L.; Liu, J. B.; Wang, H. T.; Gao, H. Evading the Strength-Ductility Trade-off Dilemma in Steel Through Gradient Hierarchical Nanotwins. *Nat. Commun.* **2014**, *5*, 3580.
(32) Ritchie, R. O. The Conflicts Between Strength and Toughness. *Nat. Mater.* **2011**, *10*, 817−822.
(33) Lu, K. The Future of Metals. *Science* **2010**, *328*, 319−320.
(34) Wegst, U. G. K.; Ashby, M. F. The Mechanical Efficiency of Natural Materials. *Philos. Mag.* **2004**, *84*, 2167−2186.
(35) Feng, J. W.; Liu, B.; Lin, Z. W.; Fu, J. Z. Isotropic Porous Structure Design Methods Based on Triply Periodic Minimal Surfaces. *Mater. Design* **2021**, *210*, No. 110050.
(36) Pun, G.; Batra, R.; Ramprasad, R.; Mishin, Y. Physically Informed Artificial Neural Networks for Atomistic Modeling of Materials. *Nat. Commun.* **2019**, *10*, 2339.
(37) Yang, Z.; Yu, C.-H.; Guo, K.; Buehler, M. J. End-to-End Deep Learning Method to Predict Complete Strain and Stress Tensors for Complex Hierarchical Composite Microstructures. *J. Mech. Phys. Solids* **2021**, *154*, No. 104506.
(38) Kim, Y.; Yang, C.; Kim, Y.; Gu, G. X.; Ryu, S. Designing an Adhesive Pillar Shape with Deep Learning-Based Optimization. *ACS Appl. Mater. Interfaces* **2020**, *12*, 24458−24465.
(39) Miscuglio, M.; Adam, G. C.; Kuzum, D.; Sorger, V. J. Roadmap on Material-Function Mapping for Photonic-Electronic Hybrid Neural Networks. *APL Mater.* **2019**, *7*, No. 100903.
(40) Chen, C.-T.; Gu, G. X. Learning Hidden Elasticity with Deep Neural Networks. *Proc. Natl. Acad. Sci.* **2021**, *118*, No. e2102721118.
(41) Zhang, Z.; Gu, G. X. Finite-Element-Based Deep-Learning Model for Deformation Behavior of Digital Materials. *Adv. Theory Simul.* **2020**, *3*, 2000031.
(42) Zheng, X. Y.; Lee, H.; Weisgraber, T. H.; Shusteff, M.; DeOtte, J.; Duoss, E. B.; Kuntz, J. D.; Biener, M. M.; Ge, Q.; Jackson, J. A.; Kucheyev, S. O.; Fang, N. X.; Spadaccini, C. M. Ultralight, Ultrastiff Mechanical Metamaterials. *Science* **2014**, *344*, 1373−1377.
(43) Alwattar, T. A.; Mian, A. Developing an Equivalent Solid Material Model for BCC Lattice Cell Structures Involving Vertical and Horizontal Struts. *J. Compos. Sci.* **2020**, *4*, 74.
(44) Deshpande, V. S.; Fleck, N. A.; Ashby, M. F. Effective Properties of the Octet-Truss Lattice Material. *J. Mech. Phys. Solids* **2001**, *49*, 1747−1769.
(45) Nye, J. F. *Physical Properties of Crystals: Their Representation by Tensors and Matrices*; Oxford University Press, New York, 1957, 322 pp..
(46) Messner, M. C. Optimal Lattice-Structured Materials. *J. Mech. Phys. Solids* **2016**, *96*, 162−183.
(47) Li, Z.; Bradt, R. C. The Single-Crystal Elastic-Constants of Cubic (3c) SiC to 1000-Degrees-C. *J. Mater. Sci.* **1987**, *22*, 2557−2559.
(48) Holec, D.; Friak, M.; Neugebauer, J.; Mayrhofer, P. H. Trends in the Elastic Response of Binary Early Transition Metal Nitrides. *Phys. Rev. B* **2012**, *85*, No. 064101.
(49) Ashby, M. F.; Medalist, R. F. M. The Mechanical-Properties of Cellular Solids. *Metall. Trans. A* **1983**, *14*, 1755−1769.
(50) Meza, L. R.; Das, S.; Greer, J. R. Strong, Lightweight, and Recoverable Three-Dimensional Ceramic Nanolattices. *Science* **2014**, *345*, 1322−1326.
(51) Lavoine, N.; Bergstrom, L. Nanocellulose-Based Foams and Aerogels: Processing, Properties, and Applications. *J. Mater. Chem. A* **2017**, *5*, 16105−16117.
(52) Cai, Z. Z.; Liu, Z. H.; Hu, X. D.; Kuang, H. K.; Zhai, J. S. The Effect of Porosity on the Mechanical Properties of 3D-Printed Triply Periodic Minimal Surface (TPMS) Bioscaffold. *Bio-Des. Manuf.* **2019**, *2*, 242−255.
(53) Weglewski, W.; Basista, M.; Manescu, A.; Chmielewski, M.; Pietrzak, K.; Schubert, T. Effect of Grain Size on Thermal Residual Stresses and Damage in Sintered Chromium-Alumina Composites: Measurement and Modeling. *Composites, Part B* **2014**, *67*, 119−124.
(54) Montemayor, L. C.; Wong, W. H.; Zhang, Y. W.; Greer, J. R. Insensitivity to Flaws Leads to Damage Tolerance in Brittle Architected Meta-Materials. *Sci. Rep.* **2016**, *6*, 20570.
(55) Mejak, G. Hashin-Shtrikman Bounds of Periodic Linear Elastic Media with Cubic Symmetry. *Math. Mech. Solids* **2020**, *25*, 1182−1198.
(56) Wang, Y. F.; Ramirez, B.; Carpenter, K.; Naify, C.; Hofmann, D. C.; Daraio, C. Architected Lattices with Adaptive Energy Absorption. *Extreme Mech. Lett.* **2019**, 33.
(57) Maconachie, T.; Leary, M.; Lozanovski, B.; Zhang, X. Z.; Qian, M.; Faruque, O.; Brandt, M. SLM Lattice Structures: Properties, Performance, Applications and Challenges. *Mater. Design* **2019**, *183*, No. 108137.
(58) *COMSOL Multiphysics®*. www.comsol.com. COMSOL AB S, Sweden.
(59) Hill, R. Elastic Properties of Reinforced Solids: Some Theoretical Principles. *J. Mech. Phys. Solids* **1963**, *11*, 357−372.

https://doi.org/10.1021/acsami.3c02746
ACS Appl. Mater. Interfaces 2023, 15, 22543−22552